

Self-Assembled H₂Nc Molecular Lattices as a Platform for Substrate-Tunable Quantum Superlattices

Adrian Bahri¹, Zhibo Kang², Ziyang Zhu³, Eric I. Altman⁴, Yu He^{2,*} and Chunjing Jia^{1†}

¹*Department of Physics, University of Florida, 2001 Museum Rd, Gainesville, FL 32611*

²*Department of Applied Physics, Yale University, New Haven, CT 06511*

³*Department of Physics, Boston College, Chestnut Hill, MA 02467*

⁴*Department of Chemical and Environmental Engineering, Yale University, New Haven, CT 06511*

Compared to van der Waals moiré systems, molecular assembly has emerged as an exciting alternative platform for superlattice engineering via heterointegration. The electronic properties of the self-assembled square lattice monolayer molecular crystal of metal-free naphthalocyanine (H₂Nc), in particular the electronic band dispersion and their tunability by metal substrates, remain less explored. Using density functional theory, supported by angle-resolved photoemission and scanning tunneling microscopy, we compare the electronic structure of a free-standing H₂Nc monolayer with that of H₂Nc lattice assembled on noble metal substrates. In the freestanding film, we identify both nearly flat, molecule-localized states and more dispersive bands, and we show that each can be compactly described by an anisotropic tight-binding Hamiltonian that yields band-resolved hopping anisotropies. We further reveal wide tunability in the Coulomb interaction and inter-site hopping based on different molecular orbitals. Adsorption on Ag(100) drives strong orbital hybridization, charge transfer, and C₂ symmetry breaking, producing partially filled, substrate-mediated dispersive states that metallize the molecular lattice. Orbital analysis identifies C₂-even and C₂-odd components and maps the spatial pattern of charge redistribution tied to symmetry breaking. Complementary ARPES on H₂Nc/Au(111) qualitatively corroborates the predicted dispersion and partial filling. These results clarify how metal substrates convert H₂Nc from isolated molecules into a tunable 2D lattice and highlight molecular superlattices as a versatile platform to simulate anisotropic lattice models.

INTRODUCTION

Moiré engineering enables a new route to quantum simulation of correlated electrons by using stacked atomic layers to create artificial superlattices. It successfully enables the simulation of topological and correlated physics such as the integer and fractional quantum anomalous Hall effects [1–3]. However, substantial spatially dependent interlayer spacing [4], structural domains [5], twist angle disorder [6], and sample-to-sample variations, preventing reproducibility at the microscopic Hamiltonian level and hinder reliable realization of targeted correlated phases.

Instead of the traditional top-down approach of mechanically stacking and twisting atomic layers, molecular frameworks (MOFs, COFs, HOFs) and supramolecular self-assembly (SSA) on solid-state surfaces offer a bottom-up route to artificial superlattices with intrinsic structural order [7–10]. Unlike moiré heterostructures, where twist angle inhomogeneity and interlayer reconstruction produce spatially varying electronic environments that are difficult to control or reproduce across devices, molecular superlattices self-assemble with a well-defined and globally uniform periodicity, offering

an intrinsically homogeneous platform. In most cases, the molecular superlattice generally weakly perturbs the itinerant substrate electronic states, causing benign hybridization gaps [11–14]. On the other hand, the molecular network itself can act as the artificial atomic lattice (“quantum dot array”), while the substrate provides means to control the intermolecular electron hopping [10, 15]. This offers a complementary route to simulate lattice models from the local limit, and is of practical relevance for molecular network-based surface interconnects and conducting films without needing manual molecule-by-molecule placement [16–19]. Here we address a matter-of-principle problem: although molecular superlattices often weakly perturb itinerant substrate states, the achievable range of electronic band dispersion within the two-dimensional molecular lattice itself remains unclear, as does the extent to which substrate electronic states renormalize its properties. In particular, we quantify the energy scale and anisotropy of intermolecular hopping in molecular superlattices and determine how these parameters can be tuned through coupling to metal substrates.

Among the most promising building blocks for such molecular lattices are conjugated macrocycles such as phthalocyanines and naphthalocyanines, which combine strong optical activity with chemically tunable frontier orbitals, making them attractive building blocks for nanoscale electronics, photonics, and sensing [20–22]. In real devices, however, the electronic character

* yu.he@yale.edu

† chunjing@phys.ufl.edu

of an isolated molecule is often dramatically reshaped by metal contacts: adsorption can change level alignment, induce charge transfer and screening, and produce new substrate-mediated electronic states [23–25]. Because contact-driven modifications can qualitatively alter transport and optical response, a quantitative understanding of how metal substrates change the electronic properties of such molecular monolayers is essential for device design and for interpreting spectroscopic measurements. Experimental and theoretical studies of phthalocyanines and related macrocycles on noble metals have documented a range of behaviors from weak physisorption to stronger hybridization and partial charge transfer at single-molecule level [26–30]. However, collective film properties, such as band formation, dispersion, and partial filling, cannot be inferred from single-molecule probes alone.

In this work, we report a combined theoretical and experimental investigation on the electronic structure of a self-assembled H_2Nc monolayer on noble metal substrates. Using first principles methods, we investigate the ground state electronic symmetry, hopping anisotropy, and on-site Coulomb repulsions in the free-standing monolayer. We then study the charge transfer and band hybridization effects when the molecules assemble on a noble metal substrate. Finally, we use angle-resolved photoemission spectroscopy (ARPES) and scanning tunneling microscopy (STM) to examine the theoretical predictions for self-assembled H_2Nc monolayers on Au(111), and reveal large charge transfer and HOMO bandwidth enhancements. Validated by both theory and experiment, the length and energy scales of such 2D molecular monolayers closely match those of moiré lattices. This alignment, combined with the ability to gate into diverse electronic bands and an expansive library of molecule-substrate combinations, establishes these networks as a highly tunable platform for quantum simulation that extends beyond current moiré systems.

RESULTS

Theoretical electronic structure of the H_2Nc monolayer

We begin with a theoretical investigation of the atomic and electronic structure of self-assembled H_2Nc 2D lattices. We focus on the arrangement where all H_2Nc molecules are oriented along the same direction, so each unit cell contains a single H_2Nc molecule, which we found to be the most energetically favorable configuration. Alternative molecular registries, which result in different overall lattice symmetries, are presented in the Supplementary Information. As seen in Fig. 1 (a), the H_2Nc molecule has two central hydrogen atoms that re-

duce the nominal C_4 symmetry of the macrocycle to C_2 , resulting in a built-in anisotropy for many electronic orbitals in the thin-film. While the lattice is nearly square ($a_y/a_x \approx 1.001$), it is still necessary to treat the X and Y directions independently, as our chosen path through the first Brillouin zone shows.

Figure 1(b) shows the electronic band structure of the relaxed free-standing monolayer and identifies the three most dispersive bands in this energy window (i-iii). Panels 1(c)-(f) focus primarily on the frontier states. The HOMO (highest occupied molecular orbital) and LUMO (lowest unoccupied molecular orbital) bands are weakly dispersive, with measured bandwidths between 3 and 4 meV. The HOMO band remains essentially isotropic, while anisotropy in the LUMO band reflects the intrinsic anisotropy of the molecule. This is further reflected in the visualized Bloch orbitals; in the thin film (panel (e)) and in a single isolated molecule (panel (f)), the HOMO has negligible amplitude near the two central hydrogens, while the LUMO has significant weight in that region. By contrast, bands labeled (i)-(iii) are significantly more delocalized and extend onto neighboring molecules, consistent with greater intermolecular hopping. These observations motivate an anisotropic nearest-neighbor tight-binding description, which we fit band-by-band in the next section.

Effective electronic parameters and Coulomb interactions

Based on the calculated electronic band dispersion and orbitals for the molecular network of H_2Nc , in this section we will derive the effective hopping parameters and the Coulomb interactions, which serve as the fundamental competing energies in most correlated materials. We express each single-particle DFT band with a minimal anisotropic tight-binding model description to obtain the hopping parameters. For short-ranged Coulomb interactions, we take maximally-localized Wannier functions (MLWF) for the HOMO band and evaluate the relevant integrals. This approach enables us to treat the kinetic and interaction energy scales and allows us to compare them directly.

For each band n we fit the dispersion to the anisotropic nearest-neighbor model:

$$H_n = \sum_{\mathbf{k}} \left[\varepsilon_n + 2t_{x,n} \cos(k_x a_x) + 2t_{y,n} \cos(k_y a_y) \right] c_{\mathbf{k}}^\dagger c_{\mathbf{k}}, \quad (1)$$

extracting the on-site energy ε_n and hoppings $t_{x,n}$, $t_{y,n}$. These fits were performed by least-squares on the DFT eigenvalues along the high-symmetry line as shown in figure 1(a), and yield high fidelity per-band (see table I in the SI). Figure 2(c) reports the fitted ε_n , $t_{x,n}$, and $t_{y,n}$ for all bands in the chosen energy window which

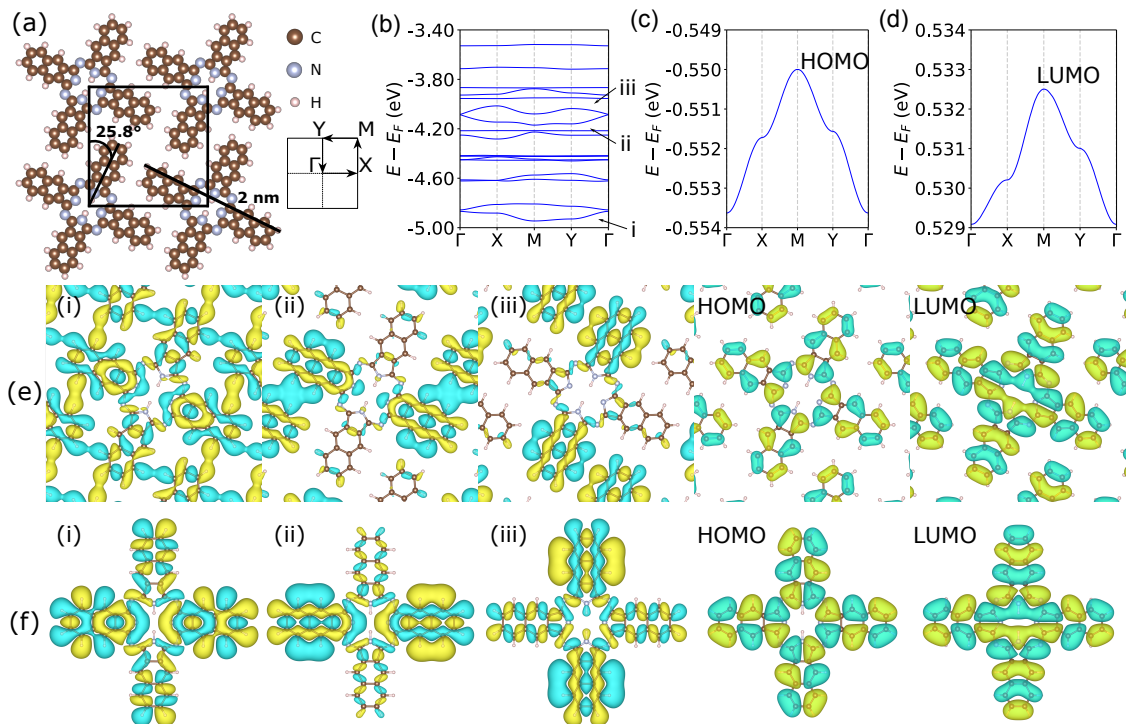


Figure 1. (a) Top view of the relaxed H₂Nc thin film and high-symmetry line through the first Brillouin zone of the anisotropic square lattice. (b) Low-energy band structure; labels i-iii mark the most dispersive low-energy bands. (c,d) HOMO and LUMO bands, respectively. (e,f) Real parts of the Γ -point Bloch orbitals for the thin film (e) and an isolated molecule (f). orbitals were prepared using vaspkit[31] and visualized using VESTA[32].

satisfy $R^2 \geq 0.98$ and provides a compact parameterization for subsequent model and transport studies. To probe the on-site Coulomb interaction term in the Hubbard model, we compute the Coulomb matrix elements for the HOMO Wannier function $w(\mathbf{r})$, following the method shown in Refs. [33, 34]. Defining the Wannier density and its Fourier transform as

$$\rho(\mathbf{r}) = |w(\mathbf{r})|^2, \quad \rho_{\mathbf{q}} = \int d^2\mathbf{r} \rho(\mathbf{r}) e^{-i\mathbf{q}\cdot\mathbf{r}}, \quad (2)$$

the interaction at lattice separation \mathbf{R} is

$$U(\mathbf{R}) = \frac{1}{(2\pi)^2} \int d^2\mathbf{q} V(\mathbf{q}) |\rho(\mathbf{q})|^2 e^{i\mathbf{q}\cdot\mathbf{R}} \quad (3)$$

We evaluate this numerically as the discrete Brillouin-zone sum

$$U_{ij} \equiv U(\mathbf{R}_{ij}) = \frac{1}{A} \sum_{\mathbf{q} \in \text{BZ}} V(\mathbf{q}) |\rho(\mathbf{q})|^2 e^{i\mathbf{q}\cdot\mathbf{R}_{ij}}, \quad (4)$$

where \mathbf{R}_{ij} is the vector from site j to site i , A is the real-space area of the supercell used, and the on-site Hubbard U is $U \equiv U_{ii} = U(\mathbf{0})$. The screening model used is

$$V(\mathbf{q}) = \frac{e^2}{2\epsilon\epsilon_0|\mathbf{q}|} \tanh(|\mathbf{q}|\xi), \quad (5)$$

where ϵ is an effective dielectric constant and ξ is the distance from the sample to the top and bottom metallic screening gates [35–37]. Further details on the numerical procedure and verification are given in the SI.

Figure 2 summarizes the calculated hopping parameters and Coulomb interactions. Panel (a) shows the HOMO MLWF isosurface used to construct the density form factor $\rho(\mathbf{q})$, as well as the definitions of on-site Coulomb U and the nearest- and next-nearest neighbor Coulomb interactions $V_{1,0}$ and $V_{1,1}$. Panel (b) displays the model geometry for screened Coulomb interactions which is represented by our interaction kernel in Eqn. (5). Panel (d) lists the computed on-site and short-range intersite Coulomb values for several choices of ϵ and ξ ; increasing ϵ or reducing ξ systematically lowers the interaction scale, as expected from metallic/dielectric screening. For the free-standing monolayer limit ($\epsilon = 1$, $\xi \rightarrow \infty$), we obtain an intrinsic on-site Hubbard $U = 3.99$ eV with short-range repulsions $V_{1,0} = 1.32$ eV and $V_{1,1} = 0.87$ eV. These values are upper bounds in the sense that additional screening from higher-energy bands or substrate image charges would reduce the effective interactions.

To assess correlation strength, the interaction scales should be compared with the kinetic energy scales ex-

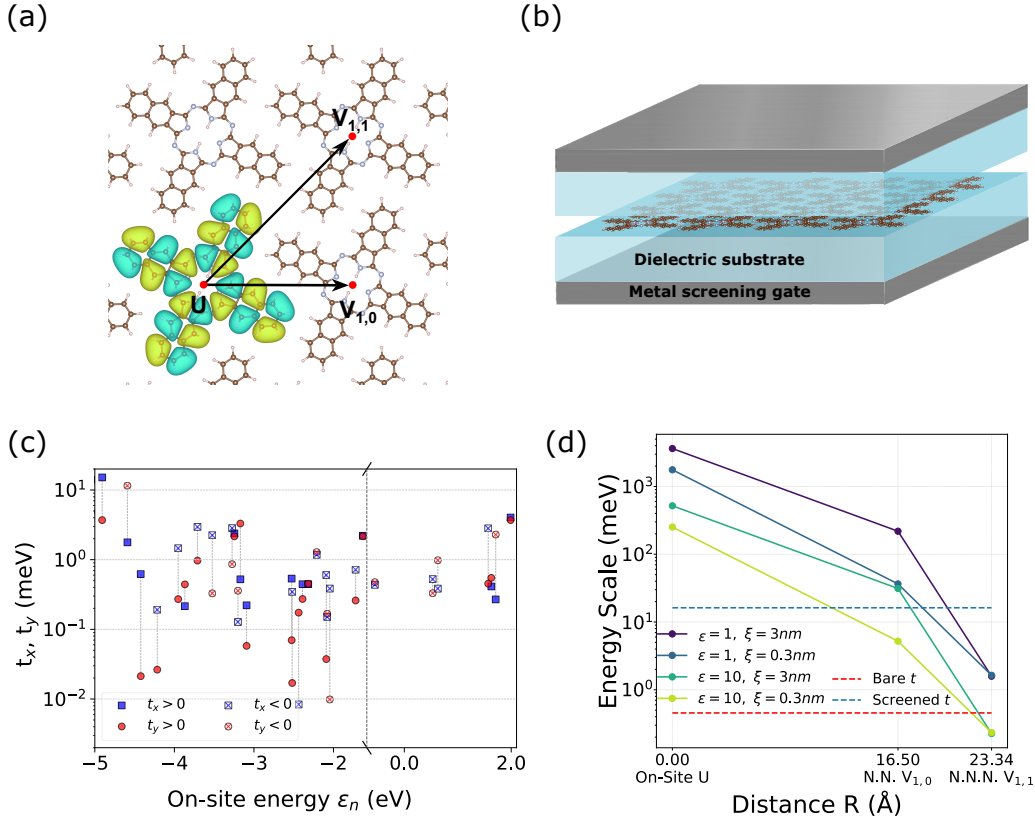


Figure 2. (a) Maximally-localized Wannier orbital for HOMO in the free-standing H₂Nc monolayer. U represents the on-site Coulomb interaction. Sites labeled $V_{1,0}$ and $V_{1,1}$ indicate the nearest- and next-nearest-neighbor vectors used to extract short-range Coulomb interactions V_{ij} . (b) Schematic of the model geometry and parameters entering the screening kernel (see text and Eqn. (5)). (c) Tight-binding parameters ϵ_n , $t_{x,n}$, and $t_{y,n}$, for the free-standing 2D thin film, for all bands in an energy window around E_F (shaded/open markers distinguish positive/negative hoppings). (d) Computed on-site U and short-range intersite V_{ij} for several choices of the effective dielectric ϵ and screening length ξ .

tracted above. Figure 2(d) also includes a “bare” and “screened” hopping t value. The bare t refers to the hopping obtained from the tight-binding fit applied to the HOMO of the free-standing thin film. The screened t is an estimated hopping parameter for the noble-metal-supported H₂Nc thin film and is obtained from the calculations described in the next section. Numerically, the bare t is very small (≈ 0.45 meV) while the on-site U values range roughly from 0.2 to 4 eV depending on the dielectric environment, giving rise to enormous bare ratios $U/t_{\text{bare}} \sim 4 \times 10^2 - 8.9 \times 10^3$. Using the substrate-estimated (screened) hopping $t_{\text{screened}} \approx 16$ meV instead, the ratios reduce to $U/t_{\text{screened}} \sim 13 - 250$. These numbers illustrate two points: (i) the intrinsic interaction scale is large compared with the freestanding kinetic scale, and (ii) substrate screening and hybridization can dramatically reduce U/t , moving the system from an extremely localized limit toward intermediate correlation regimes.

Substrate-mediated band modulation in H₂Nc monolayers

Having established the intrinsic electronic properties of the free-standing H₂Nc thin film, we now examine how these are modified upon adsorption on Ag(100), as summarized in Fig. 3. Panels (a) and (b) compare the projected band structures and DOS for the isolated monolayer and the adsorbed film. In contrast to the free-standing case, where the DOS vanishes at the Fermi level, adsorption produces partially filled, dispersive states with substantial molecular character. These states appear as broadened molecular resonances which hybridize with Ag states, leading to both peak broadening and energy shifts. The reference DOS of the bare Ag(100) slab (Fig. 3 (b)) differs substantially from the DOS of the combined system, showing that the electronic structure of the adsorbed film is distinct from both the freestanding H₂Nc monolayer and the bare

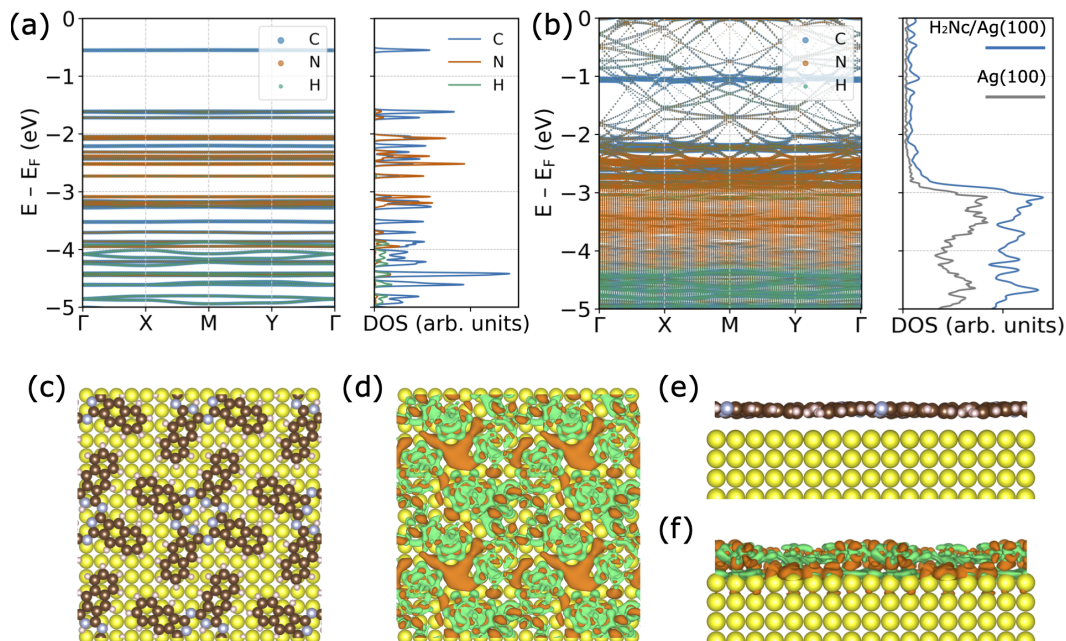


Figure 3. (a) Projected band structure and density of states (DOS) of the free-standing H_2Nc monolayer and (b) the monolayer adsorbed on $\text{Ag}(100)$. A Gaussian smearing of 20 meV has been applied to all DOS curves. The reference DOS for the bare $\text{Ag}(100)$ slab is also shown. (c,e) Top and side views of the relaxed $\text{H}_2\text{Nc}/\text{Ag}(100)$ geometry. Further structure characterization can be found in the supplementary material. (d,f) Top and side views of the bonding charge density difference, with isosurfaces shown at $3 \times 10^{-4} e^-/\text{\AA}^3$. Orange represents electron accumulation and green shows depletion.

$\text{Ag}(100)$ slab. The screened hopping $t = 16.2$ meV reported in Fig. 2 (d) is estimated from the HOMO spectral width by taking the FWHM of the HOMO peak in the DOS in Fig. 3 (b) as an approximate bandwidth W and using $t \approx W/8$ for a square lattice. In a physical system, increased hopping due to substrate-molecule interaction will also make the MLWF more delocalized, decreasing the on-site Coulomb interaction and further reducing U/t . By appropriate tuning of metal substrate, film-substrate spacing, or dielectric environment, one can therefore tune t and U (and hence U/t) over many orders of magnitude, enabling exploration of weakly to strongly correlated regimes.

Fig. 3(c) and (e) show the relaxed adsorption geometry; adsorption on the fcc $\text{Ag}(100)$ surface breaks the nominal C_2 rotational symmetry of the freestanding molecular layer. To visualize the interfacial charge rearrangement, Fig. 3 (d) and (f) plot the bonding charge-density difference $\Delta\rho(\mathbf{r}) = \rho_{\text{combined}}(\mathbf{r}) - \rho_{\text{slab}}(\mathbf{r}) - \rho_{\text{molecule}}(\mathbf{r})$. Orange (accumulation) and green (depletion) isosurfaces highlight regions of net gain and loss of electronic density; accumulation is found in the interstitial regions and around the macrocycle, while the molecular arms are depleted. The isosurfaces are plotted at $\Delta\rho = 3 \times 10^{-4} e^-/\text{\AA}^3$, indicating a spatially extended but modest charge redistribution consistent with ph-

ysisorption of π -conjugated molecules on silver[38, 39].

To quantify the charge redistribution visible in Fig. 3 (d) and (f), we performed a Bader charge analysis on the relaxed combined slab+molecular geometry[40–43]. The Bader partitioning yields a net transfer of ≈ 1.46 electrons per molecule from the Ag substrate to the H_2Nc film. The transferred charge is not uniformly distributed across the molecule: nitrogen centers capture the majority of the gain (mean $\Delta q \approx +0.83 e^-$ per N), hydrogen atoms show a small electron gain (mean $\Delta q \approx 0.14 e^-$ per H), and carbon atoms show a small depletion (mean $\Delta q \approx -0.186 e^-$ per C).

Experimental observation of substrate-tunable dispersion

The electronic structure modification due to substrate-molecule interaction is investigated experimentally with angle-resolved photoemission spectroscopy (ARPES) and scanning tunneling microscopy (STM). Monolayer H_2Nc is grown on sputter-annealed $\text{Au}(111)$ surface via a home-built molecular beam epitaxy system. Figure 4(a) shows the low energy electronic density of states (DOS) on pristine $\text{Au}(111)$ and $\text{H}_2\text{Nc}/\text{Au}(111)$ measured under He $I\alpha$ line (21.2

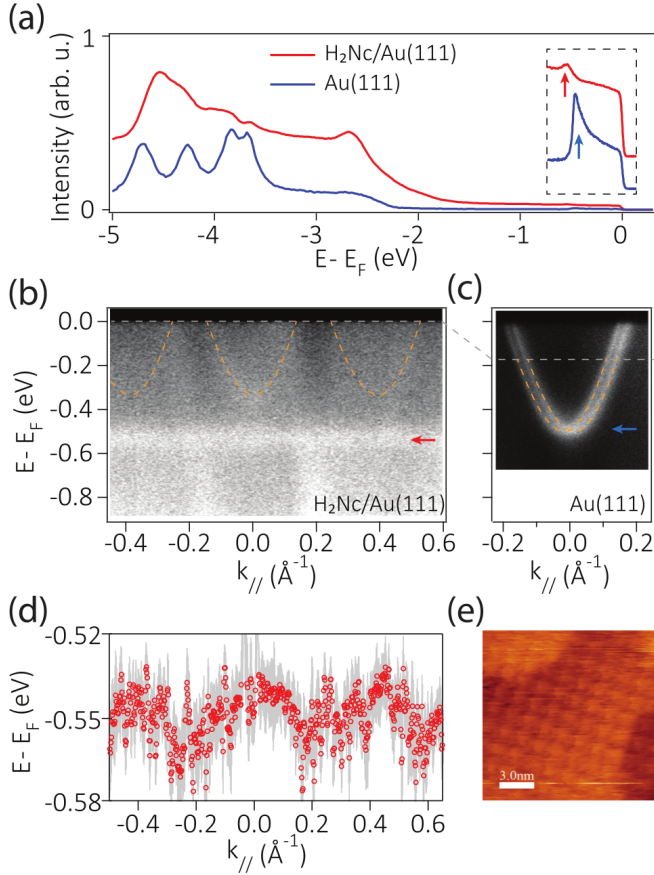


Figure 4. Electronic structure of H₂Nc self-assembly on Au(111). (a) Comparison of UPS spectra of pristine Au(111) surface and H₂Nc monolayer. Inset shows high-resolution zoom-in view of the low-energy electronic states. Red arrow denotes the HOMO band, and blue arrow denotes the Shockley surface state band bottom. Energy-momentum cuts through Γ on (b) sub-monolayer H₂Nc/Au(111) and (c) pristine Au(111) surface. Yellow dashed lines denote the Shockley surface state of Au(111). (d) Fitted dispersion of the HOMO band. (e) Topographic image of local patches of self-assembled H₂Nc on Au(111).

eV). Compared to Fig. 4(a), the spectral density of H₂Nc/Au(111) is substantially modified from that of Au(111), while retaining the envelope shape of eV-scale DOS distribution of Au(111). This already indicates strong electronic mixing between the molecule layer and metal substrate, which is further bolstered by the energy-momentum spectra shown in Fig. 4(b) and (c). The Shockley surface state (orange dash) can still be resolved in the case of H₂Nc/Au(111) especially near Γ [44], and is notably depleted by ~ 200 meV due to substantial electron transfer from Au(111) to the H₂Nc network, consistent with the Bader analysis in the previous section. As a result, the HOMO band of H₂Nc sits roughly 550 meV below the chemical potential (red

arrow, also shown in Fig. 4(a) inset).

The superlattice potential exerted by the H₂Nc network on the Au(111) surface is also visible through the faint Umklapp replicas of the Shockley state in momentum space, with the momentum scattering vector matching the reciprocal lattice vector of the H₂Nc assembly measured by STM (Fig. 4(e)). Intriguingly, the dispersion bandwidth of the HOMO band not only shows a periodic oscillation according to the molecular lattice, but also exhibits a bandwidth of about 50 meV, an order of magnitude larger than that of a free-standing H₂Nc film (Table I). This qualitatively matches the expected electron kinetic energy enhancement due to strong hybridization with metal conduction electrons, as calculated for the H₂Nc/Ag(100) interface in Fig. 3(b). Compared to previous molecular assembly studies using substantially larger molecules, the H₂Nc lattice adopted here measures above the typical Fermi wavelength of the Shockley surface state electron gas, which avoided direct Umklapp band hybridization seen in other systems [10]. Finally, due to the tautomerization associated with the inner two hydrogen atoms' position fluctuations – due to both thermal activation and quantum tunneling [45, 46] – the in-plane dispersion anisotropy is not expected in these measurements at liquid nitrogen temperatures.

CONCLUSION AND DISCUSSION

We used first-principles calculations and surface spectroscopy to quantify how intermolecular hopping, band dispersion, and Coulomb interactions in self-assembled H₂Nc monolayers are modified by metal substrates. Tight-binding fits of the free-standing film's electronic band structure reveal very small intrinsic hoppings and correspondingly large on-site Coulomb energies (intrinsic U up to 3.99 eV). When the film is supported on a noble metal, metallic screening and hybridization substantially enhance effective hopping and reduce U/t , as confirmed by ARPES which shows a significantly broadened HOMO band compared to the thin film. Our calculations show that substrate choice, film-substrate spacing, and dielectric environment can tune U/t across orders of magnitude, enabling exploration of weakly to strongly correlated regimes with the same molecular film.

These results highlight the molecular assembly/solid state interface as an exciting platform to engineer electronic properties: on the one hand, the molecules can act upon the solid state surface via a superlattice potential, creating mini Brillouin zones akin to those in moiré engineered systems but in an *in situ* scalable way; on the other hand, the metal substrate can interact strongly with the periodic molecular lattice, causing enhanced electron hopping across molecules, and poten-

tially be exploited to modify the optical and magnetic response of such molecular thin films. Recent developments on *in situ* growth of molecular thin films over van der Waals substrates demonstrated pronounced moiré superlattice effects on the optical properties of the substrates, validating this new route of molecular superlattice engineering to design, create, and control new quantum material properties [47, 48].

METHODS

Density Functional Theory Calculations

In order to compute the desired electronic properties of the various structures studied, first-principles density functional theory (DFT) calculations were performed using the Vienna *ab-initio* Simulation Package (VASP)[49, 50]. Projector-augmented wave (PAW) potentials [51] were used to implement the generalized gradient approximation (GGA) and correlation effects were implemented using the revised PBE from Zhang and Yang [52]. Dispersion interactions between nearby molecules in the H₂Nc system and between the molecular layer and the substrate were accounted for using the DFT-D3 method of Grimme et al. with Becke–Johnson damping [53, 54]. This choice of van-der-Waals functionals results in good agreement of the lattice parameters with experimental values [55]. Wannier downfolding is implemented using maximally localized Wannier functions with Wannier90 [56].

Isolated H₂Nc Thin Film

Calculations for the isolated H₂Nc monolayer were done using a plane-wave basis set of energy cutoff 480 eV and an $11 \times 11 \times 1$ Monkhorst-Pack (MP) k-point mesh. The structural relaxation of both atomic positions and lattice parameters was performed until residual forces on all atoms were less than 5 meV/Å. Vacuum space of 20 Å was maintained in the *c* direction in order to generate an isolated monolayer. The electronic band structure, density of states, and Γ -point Bloch wavefunctions were generated from calculations using a Gaussian smearing of 20 meV.

Molecular Layer on Ag(100) Substrate

DFT calculation was performed to find the lattice constant of bulk Ag(100) to be 4.07 Å, which agrees well with the high-precision experimentally measured value of 4.08 Å[57]. A compressive strain of about 1%

was then applied to the relaxed H₂Nc thin film in order to commensurately place it above a $4 \times 4 \times 2$ slab of Ag(100) (lattice parameters $a = b = 16.29$ Å). The Ag(100) slab was placed at the center of a periodic cell with the H₂Nc layer 3 Å above it, with 15 Å of vacuum below the bottom Ag layer and 12 Å of vacuum above the molecular film to fully decouple periodic images. The lowest-energy placement of the molecular layer on the substrate was found by applying rigid translations of the fully relaxed H₂Nc monolayer over the substrate in fractional steps of 0.25 Ag lattice constants, or about 1 Å resolution, in the [100], [010], and [110] directions, and performing Γ -point relaxations of the *z*-components of the atomic positions within the molecular layer to a force convergence of 0.01 eV/Å. The energy difference between the highest and lowest energy placements of the molecular layer was approximately 140 meV, highlighting the importance of this grid search procedure. After choosing the lowest energy placement, all degrees of freedom of the atoms within the molecular layer and top two substrate layers were relaxed with an $11 \times 11 \times 1$ MP-mesh to a force convergence of 0.01 eV/Å. Further structure characterization of the thin film, free-standing and adsorbed on Ag(100), can be found in the supplementary material.

Using the fully relaxed geometry, calculations were performed to obtain the band structure, density of states, and bonding charge density difference of the substrate and H₂Nc layer. Because the structure contains both a bulk metal and an insulating molecular layer, a series of exploratory calculations using Gaussian smearing widths ranging from 50 meV down to 2 meV were performed to confirm robustness of the results to changes in smearing. Essentially identical results were obtained for all such calculations, and those presented correspond to a smearing of 20 meV.

Growth of Naphthalocyanine on Au(111) Substrate

The growth was carried out in a homemade ultra-high vacuum (UHV) molecular beam epitaxy (MBE) system with a base pressure better than 1.5×10^{-10} Torr. A single-crystal Au(111) (roughness < 0.01 μm , orientation accuracy < 0.1°, Princeton Scientific) was prepared in the UHV MBE chamber by repeated cycles of argon sputtering and subsequent annealing at 500°C until a clean surface was confirmed by reflective high-energy electron diffraction (RHEED) or Auger electron spectroscopy (AES). Purified H₂Nc in powder form was degassed at 390°C for 1 hour under UHV using a Knudsen cell (Rocksteady). It was evaporated at 390°C with the Au(111) substrate kept at room temperature. The evaporation rate was about 0.2 layers per minute monitored by a quartz crystal microbalance (Inficon).

Structural and Spectroscopic Characterization

The structure of the film was characterized in situ by a homemade scanning tunneling microscope (STM) using a Pt-Ir tip in constant-current mode. Angle-resolved photoemission spectroscopy experiment was carried out in situ in a homemade system under UHV about 4×10^{-11} Torr. ARPES data were collected using the MB Scientific A-1 analyzer. Monochromatized 21.2 eV VUV light was generated by a helium discharge lamp (SPECS UVS 300) delivered to the same surface via an ellipsoidal focusing capillary.

ACKNOWLEDGMENTS

We thank Sam Trickey for the insightful discussion. This work is supported by the Center for Molecular

Magnetic Quantum Materials, an Energy Frontier Research Center funded by the U.S. Department of Energy, Office of Science, Basic Energy Sciences under Award no. DE-SC0019330. Computations were done using the utilities of the University of Florida Research Computing. Y.H. and Z.K. acknowledge the support of the Office of Naval Research (ONR) under grant No. N0014-23-1-2018. EIA acknowledges the support of the National Science Foundation through grant number CHE-2203589. ZZ acknowledges a startup fund at Boston College.

-
- [1] F. Xu, Z. Sun, T. Jia, C. Liu, C. Xu, C. Li, Y. Gu, K. Watanabe, T. Taniguchi, B. Tong, J. Jia, Z. Shi, S. Jiang, Y. Zhang, X. Liu, and T. Li, *Phys. Rev. X* **13**, 031037 (2023).
- [2] H. Park, J. Cai, E. Anderson, Y. Zhang, J. Zhu, X. Liu, C. Wang, W. Holtzmann, C. Hu, Z. Liu, T. Taniguchi, K. Watanabe, J.-H. Chu, T. Cao, L. Fu, W. Yao, C.-Z. Chang, D. Cobden, D. Xiao, and X. Xu, *Nature* **622**, 74 (2023).
- [3] Y. Zeng, Z. Xia, K. Kang, J. Zhu, P. Knüppel, C. Vaswani, K. Watanabe, T. Taniguchi, K. F. Mak, and J. Shan, *Nature* **622**, 69 (2023).
- [4] T. Devakul, V. Crépel, Y. Zhang, and L. Fu, *Nature Communications* **12**, 6730 (2021).
- [5] H. Yoo, R. Engelke, S. Carr, S. Fang, K. Zhang, P. Cazeaux, S. H. Sung, R. Hovden, A. W. Tsen, T. Taniguchi, K. Watanabe, G.-C. Yi, M. Kim, M. Luskun, E. B. Tadmor, E. Kaxiras, and P. Kim, *Nature Materials* **18**, 448 (2019).
- [6] A. Uri, S. Grover, Y. Cao, J. A. Crosse, K. Bagani, D. Rodan-Legrain, Y. Myasoedov, K. Watanabe, T. Taniguchi, P. Moon, *et al.*, *Nature* **581**, 47 (2020).
- [7] S. E. Freeney, M. R. Slot, T. S. Gardenier, I. Swart, and D. Vanmaekelbergh, *ACS Nanoscience Au* **2**, 198 (2022).
- [8] R. Yin, X. Zhu, Q. Fu, T. Hu, L. Wan, Y. Wu, Y. Liang, Z. Wang, Z.-L. Qiu, Y.-Z. Tan, C. Ma, S. Tan, W. Hu, B. Li, Z. F. Wang, J. Yang, and B. Wang, *Nature Communications* **15**, 2969 (2024).
- [9] C.-Y. Chen, E. Li, H. Xie, J. Zhang, J. W. Y. Lam, B. Z. Tang, and N. Lin, *Communications Materials* **5**, 54 (2024).
- [10] I. Piquero-Zulaica, J. Lobo-Checa, Z. M. A. El-Fattah, J. E. Ortega, F. Klappenberger, W. Auwärter, and J. V. Barth, *Rev. Mod. Phys.* **94**, 045008 (2022).
- [11] I. Piquero-Zulaica, J. Li, Z. M. Abd El-Fattah, L. Solianyk, I. Gallardo, L. Monjas, A. K. H. Hirsch, A. Arnau, J. E. Ortega, M. Stöhr, and J. Lobo-Checa, *Nanoscale* **11**, 23132 (2019).
- [12] I. Piquero-Zulaica, A. Sadeghi, M. Kherelden, M. Hua, J. Liu, G. Kuang, L. Yan, J. E. Ortega, Z. M. A. El-Fattah, B. Azizi, N. Lin, and J. Lobo-Checa, *Phys. Rev. Lett.* **123**, 266805 (2019).
- [13] T. Ules, D. Lüftner, E. M. Reinisch, G. Koller, P. Puschnig, and M. G. Ramsey, *Phys. Rev. B* **90**, 155430 (2014).
- [14] C.-S. Zhou, X.-R. Liu, Y. Feng, X. Shao, M. Zeng, K. Wang, M. Feng, and C. Liu, *Applied Physics Letters* **117**, 191601 (2020).
- [15] I. Piquero-Zulaica, J. Li, Z. M. Abd El-Fattah, L. Solianyk, I. Gallardo, L. Monjas, A. K. H. Hirsch, A. Arnau, J. E. Ortega, M. Stöhr, and J. Lobo-Checa, *Nanoscale* **11**, 23132 (2019).
- [16] J. Shang, Y. Wang, M. Chen, J. Dai, X. Zhou, J. Kuttner, G. Hilt, X. Shao, J. M. Gottfried, and K. Wu, *Nature Chemistry* **7**, 389 (2015).
- [17] M. R. Slot, T. S. Gardenier, P. H. Jacobse, G. C. P. van Miert, S. N. Kempkes, S. J. M. Zevenhuizen, C. M. Smith, D. Vanmaekelbergh, and I. Swart, *Nature Physics* **13**, 672 (2017).
- [18] C.-Y. Chen, E. Li, H. Xie, J. Zhang, J. W. Y. Lam, B. Z. Tang, and N. Lin, *Communications Materials* **5**, 54 (2024).
- [19] R. Yin, X. Zhu, Q. Fu, T. Hu, L. Wan, Y. Wu, Y. Liang, Z. Wang, Z.-L. Qiu, Y.-Z. Tan, C. Ma, S. Tan, W. Hu, B. Li, Z. F. Wang, J. Yang, and B. Wang, *Nature Communications* **15**, 2969 (2024).
- [20] O. Opeyemi, H. Louis, C. Opara, O. Funmilayo, and T. Magu, *Advanced Journal of Chemistry-Section A* , 21–44 (2019).
- [21] O. A. Melville, B. H. Lessard, and T. P. Bender, *ACS Applied Materials & Interfaces* **7**, 13105 (2015), PMID: 26000612, <https://doi.org/10.1021/acsami.5b01718>.

- [22] E. Menard, M. A. Meitl, Y. Sun, J.-U. Park, D. J.-L. Shir, Y.-S. Nam, S. Jeon, and J. A. Rogers, *Chemical Reviews* **107**, 1117 (2007), pMID: 17428024, <https://doi.org/10.1021/cr050139y>.
- [23] T. G. Gopakumar, M. Lackinger, M. Hackert, F. Müller, and M. Hietschold, *The Journal of Physical Chemistry B* **108**, 7839 (2004), <https://doi.org/10.1021/jp037751i>.
- [24] H. Yamane, A. Carlier, and N. Kosugi, *Materials Chemistry Frontiers* **2**, 609 (2018).
- [25] W. Dou, S. Huang, R. Zhang, and C. S. Lee, *The Journal of chemical physics* **134** (2011).
- [26] Z. Li, B. Li, J. Yang, and J. G. Hou, *Accounts of Chemical Research* **43**, 954 (2010), pMID: 20359193, <https://doi.org/10.1021/ar9001558>.
- [27] I. Kröger, B. Stadtmüller, C. Kleimann, P. Rajput, and C. Kumpf, *Phys. Rev. B* **83**, 195414 (2011).
- [28] J. Granet, M. Sicot, I. C. Gerber, G. Kremer, T. Pierron, B. Kierren, L. Moreau, Y. Fagot-Revurat, S. Lamare, F. Chérioux, and D. Malterre, *The Journal of Physical Chemistry C* **124**, 10441 (2020), <https://doi.org/10.1021/acs.jpcc.9b11141>.
- [29] R. Wu, L. Yan, D.-L. Bao, J. Ren, S. Du, Y. Wang, Q. Huan, and H.-J. Gao, *The Journal of Physical Chemistry C* **123**, 7202 (2019), <https://doi.org/10.1021/acs.jpcc.9b00095>.
- [30] Y. Bai, F. Buchner, M. T. Wendahl, I. Kellner, A. Bayer, H.-P. Steinrück, H. Marbach, and J. M. Gottfried, *The Journal of Physical Chemistry C* **112**, 6087 (2008), <https://doi.org/10.1021/jp711122>.
- [31] V. Wang, N. Xu, J.-C. Liu, G. Tang, and W.-T. Geng, *Computer Physics Communications* **267**, 108033 (2021).
- [32] K. Momma and F. Izumi, *Journal of Applied Crystallography* **44**, 1272 (2011).
- [33] V. V. Mazurenko, S. L. Skorniyakov, A. V. Kozhevnikov, F. Mila, and V. I. Anisimov, *Phys. Rev. B Condens. Matter Mater. Phys.* **75** (2007).
- [34] T. Kariyado, A. Vishwanath, and Z.-X. Luo, *Phys. Rev. B* **112** (2025).
- [35] T. Cea, N. R. Walet, and F. Guinea, *Phys. Rev. B* **100** (2019).
- [36] J. Kang and O. Vafek, *Phys. Rev. B* **102** (2020).
- [37] T. Cea and F. Guinea, *Phys. Rev. B* **102** (2020).
- [38] C. Park, G. A. Rojas, S. Jeon, S. J. Kelly, S. C. Smith, B. G. Sumpter, M. Yoon, and P. Maksymovych, *Phys. Rev. B* **90**, 125432 (2014).
- [39] R. Otero, R. Miranda, and J. M. Gallego, *ACS Omega* **4**, 16906 (2019), pMID: 31646237, <https://doi.org/10.1021/acsomega.9b02154>.
- [40] W. Tang, E. Sanville, and G. Henkelman, *J. Phys. Condens. Matter* **21**, 084204 (2009).
- [41] E. Sanville, S. D. Kenny, R. Smith, and G. Henkelman, *J. Comput. Chem.* **28**, 899 (2007).
- [42] G. Henkelman, A. Arnaldsson, and H. Jónsson, *Computational Materials Science* **36**, 354 (2006).
- [43] M. Yu and D. R. Trinkle, *J. Chem. Phys.* **134**, 064111 (2011).
- [44] W. Shockley, *Physical review* **56**, 317 (1939).
- [45] R. Wu, D.-L. Bao, L. Yan, Y. Wang, J. Ren, Y.-F. Zhang, Q. Huan, Y.-Y. Zhang, S. Du, S. T. Pantelides, and H.-J. Gao, *The Journal of Physical Chemistry Letters* **11**, 1536 (2020).
- [46] B. Doppagne, T. Neuman, R. Soria-Martinez, L. E. P. López, H. Bulou, M. Romeo, S. Berciaud, F. Scheurer, J. Aizpuru, and G. Schull, *Nat. Nanotechnol.* **15**, 207 (2020).
- [47] T. Chowdhury, A. Champagne, P. Knüppel, Z. Naqvi, A. Ray, M. Gao, D. A. Muller, N. Guisinger, K. F. Mak, J. B. Neaton, *et al.*, arXiv preprint arXiv:2502.13460 (2025).
- [48] T. Chowdhury, F. Mujid, Z. Naqvi, A. Ray, C. Liang, D. A. Muller, N. P. Guisinger, and J. Park, *Nano Letters* **25**, 5852 (2025).
- [49] G. Kresse and J. Furthmüller, *Computational Materials Science* **6**, 15 (1996).
- [50] G. Kresse and J. Furthmüller, *Phys. Rev. B* **54**, 11169 (1996).
- [51] G. Kresse and D. Joubert, *Phys. Rev. B* **59**, 1758 (1999).
- [52] Y. Zhang and W. Yang, *Phys. Rev. Lett.* **80**, 890 (1998).
- [53] S. Grimme, J. Antony, S. Ehrlich, and H. Krieg, *The Journal of Chemical Physics* **132**, 154104 (2010), https://pubs.aip.org/aip/jcp/article-pdf/doi/10.1063/1.3382344/15684000/154104_1_online.pdf.
- [54] S. Grimme, S. Ehrlich, and L. Goerigk, *Journal of Computational Chemistry* **32**, 1456 (2011), <https://onlinelibrary.wiley.com/doi/pdf/10.1002/jcc.21759>.
- [55] T. Pham, F. Song, and M. Stöhr, *PCCP : Physical Chemistry Chemical Physics* **16**, 8881 (2014).
- [56] A. A. Mostofi, J. R. Yates, G. Pizzi, Y. S. Lee, I. Souza, D. Vanderbilt, and N. Marzari, *Computational Physics Communications* **185**, 2309 (2014), online journal.
- [57] W. P. Davey, *Phys. Rev.* **25**, 753 (1925).
- [58] R. Wu, L. Yan, Y. Zhang, J. Ren, D. Bao, H. Zhang, Y. Wang, S. Du, Q. Huan, and H.-J. Gao, *The Journal of Physical Chemistry C* **119**, 8208 (2015).
- [59] P. Mehring, A. Beimborn, T. Lühr, and C. Westphal, *The Journal of Physical Chemistry C* **116**, 12819 (2012).

ε_n (eV)	$t_{x,n}$ (meV)	$t_{y,n}$ (meV)	R^2
-2.318	0.446	0.451	0.987
-2.211	-1.172	-1.285	0.999
-2.091	-0.602	0.037	0.999
-2.080	-0.151	-0.168	0.999
-2.046	-0.385	-0.010	0.995
-1.722	-0.718	0.260	0.987
-1.631	2.197	2.167	0.998
-1.614	-0.178	-0.773	0.971
-0.552	-0.435	-0.475	0.997
0.531	-0.526	-0.330	0.996
0.627	-0.384	-0.981	1.000
1.368	-0.047	-0.134	0.947
1.569	-2.814	0.452	0.998
1.628	0.413	0.547	0.989
1.710	0.269	-2.293	0.998
1.988	4.026	3.699	0.999

Table I. Tight-binding parameters ε_n , $t_{x,n}$, and $t_{y,n}$, for the 16 bands nearest to E_F .

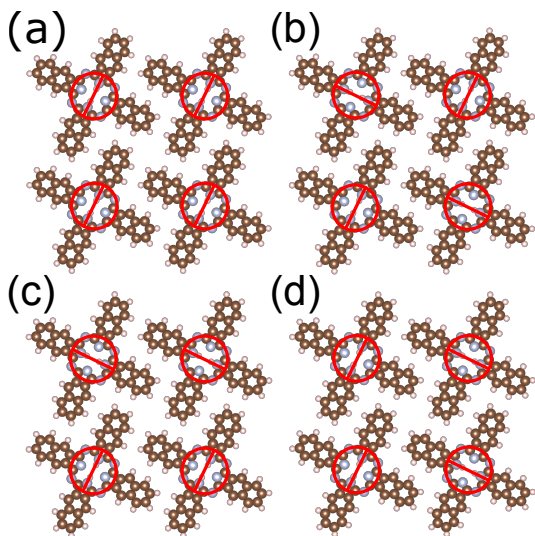


Figure 5. Different molecular configurations studied by density functional theory. We refer to them as (a): $(0,0)$, (b): (π,π) , (c): $(\pi,0)$, (d): $(0,\pi)$ orders. Red circles over the macrocycles with inscribed lines emphasize hydrogen atom orientations. The $(0,0)$ order was found to be lowest in energy by about 25 meV/molecule.

SUPPLEMENTARY MATERIALS

Structure Characterization

Exploratory DFT calculations were carried out to probe the orientations of the central hydrogen atoms within the H_2Nc macrocycle in the ground state of the thin film. Figure 5 shows the four unique periodic orientations investigated. Atomic positions and lattice parameters of the H_2Nc thin film were relaxed in configuration (a) with calculation parameters detailed in the Methods. From this structure, configurations (b), (c), and (d) were generated, and atomic positions and lattice parameters were relaxed in each configuration to a convergence threshold of 5 meV/Å.

After relaxation, the resulting lattice parameters for the isolated H_2Nc layer were approximately 16.5 Å in the a and b directions. Each molecule is approximately 2 nm wide and forms an angle of 25.8° with the lattice vectors. The relaxed structure of the free-standing H_2Nc molecules can be seen in figure

After fully relaxing the thin film on the substrate, the mean height between the top layer of the substrate and the thin film was 3.07 Å, and the range of atomic z -coordinates within the thin film was 0.52 Å. These results resemble those of Wu et al. for metal-free H_2Nc on $\text{Ag}(111)$ [58] and those of Mehring et al. for metal-free H_2Nc on $\text{Au}(100)$ [59].

It is worth noting that Mehring et al. grew the H_2Nc layer with an angle $\theta = 0^\circ$ with respect to the substrate, meaning the lobes of each molecule were aligned parallel to the lattice vectors of the substrate, while in this work $\theta = 25.8^\circ$. The structure was arranged as such for this work in order to minimize the size of the periodic unit cell and thus decrease the associated computational cost. Rotating the H_2Nc layer by a non-high-symmetry angle breaks commensurability with the $\text{Ag}(100)$ lattice. To accurately study that system would require either heavily straining the molecular film or constructing a large supercell to model the resulting Moiré pattern.

Bands and Bloch Wavefunctions

One may also notice that the parity of the wavefunctions (symmetric/antisymmetric) flips for some of the orbitals in Figure 1 between the film and the isolated molecule. Because the Bloch states at Γ in the film are formed by periodic combinations of molecular orbitals, near-degenerate levels can recombine into bonding/antibonding mixtures which differ in local parity relative to the isolated molecule. This apparent parity flip is a numerical consequence of the arbitrary orthonormal basis returned by diagonalization in a near-degenerate subspace; physical observables are unaf-

fected.

Coulomb Interactions Calculation Method

We computed Coulomb integrals for the HOMO maximally localized Wannier function $w(\mathbf{r})$ following two independent numerical routes implemented in our analysis notebook: (i) a fast Fourier-transform (FFT) method used to generate the full two-dimensional interaction map $U(\mathbf{R})$, and (ii) a direct real-space pairwise summation used as an independent check for on-site and short-range values. In the FFT method we form the in-plane density $\rho_2(x, y) = \int dz |w(x, y, z)|^2$ on the real-space grid exported from the Wannier/XSF

file, center the density to sub-pixel accuracy using an FFT phase-shift of the complex amplitude, truncate the original XSF grid to a box enclosing the orbital, then zero-pad the truncated density by integer pad factors to increase the in-plane supercell L (smallest Fourier wavevector $q_{\min} = 2\pi/L$). The 2D Fourier transform $\rho_{\mathbf{q}}$ was computed with NumPy's `fft2`, the screened interaction kernel $V(\mathbf{q})$ in Eqn. (5) was evaluated on the discrete \mathbf{q} mesh, and $U(\mathbf{R})$ was obtained by inverse FFT of $V(\mathbf{q})|\rho_{\mathbf{q}}|^2$. Analytic small- \mathbf{q} handling was used to avoid singular division by $|\mathbf{q}|$. For the free-standing limit ($\xi \rightarrow \infty$) we performed calculations for a sequence of pad factors and extrapolated the finite- L results to $L \rightarrow \infty$ by fitting $U(\mathbf{L}) = U_{\infty} + a/L$. Finite- ξ results presented in this paper were computed with a pad factor of 8.